



THE UNIVERSITY *of* EDINBURGH

Edinburgh Research Explorer

## A hybrid scheme for simulation of planar rigid bodies with impacts and friction using impact mappings

**Citation for published version:**

Burns, SJ & Piiroinen, PT 2015, 'A hybrid scheme for simulation of planar rigid bodies with impacts and friction using impact mappings', *International journal of non-Linear mechanics*, vol. 77, 2552, pp. 312-324. <https://doi.org/10.1016/j.ijnonlinmec.2015.09.011>

**Digital Object Identifier (DOI):**

[10.1016/j.ijnonlinmec.2015.09.011](https://doi.org/10.1016/j.ijnonlinmec.2015.09.011)

**Link:**

[Link to publication record in Edinburgh Research Explorer](#)

**Document Version:**

Peer reviewed version

**Published In:**

International journal of non-Linear mechanics

**General rights**

Copyright for the publications made accessible via the Edinburgh Research Explorer is retained by the author(s) and / or other copyright owners and it is a condition of accessing these publications that users recognise and abide by the legal requirements associated with these rights.

**Take down policy**

The University of Edinburgh has made every reasonable effort to ensure that Edinburgh Research Explorer content complies with UK legislation. If you believe that the public display of this file breaches copyright please contact [openaccess@ed.ac.uk](mailto:openaccess@ed.ac.uk) providing details, and we will remove access to the work immediately and investigate your claim.



# A hybrid scheme for simulation of planar rigid bodies with impacts and friction using impact mappings

Shane J. Burns\*, Petri T. Piiroinen

*School of Mathematics, Statistics & Applied Mathematics,  
National University of Ireland, Galway,  
University Road, Galway, Ireland*

---

## Abstract

This article introduces numerical techniques necessary for the implementation of impact maps derived from an energetic impact law for rigid-body impacts with friction at isolated contact points. In particular the work focuses on methodologies for long-term simulation with behaviours such as dynamic transitions and chatter. The methods are based on hybrid event-driven numerical solvers for ordinary differential equations together with system states to deal with the transitions. A slender rod impacting a periodically oscillating surface is used as an example to illustrate implementation and methods. The numerical scheme for the rod system is used to show how symmetry can play an important role in the presence of friction for long-term dynamics. This will show that surface oscillations with low frequencies tend to lead to periodic motions of the rod that are independent of friction. For higher frequencies however the periodic solutions are not that common and irregular motion ensues.

---

## 1. Introduction

Collisions or impacts in mechanical systems are very common and in many mechanical engineering applications they can cause undesired wear and noise and thus be very problematic and expensive. Two experimental examples of systems with such issues include an engine cam follower [32] and a magnetic bearing system [22].

In many applications energy is dissipated during impacts through motion in both the normal and tangential direction (friction) and how this happens has wide reaching effects on both the short-term and long-term dynamics. The understanding of the forces and impulses that occur at impact, together with an *impact law*, allows for some prediction of post-impact dynamics of impacting systems. By an impact law we mean a physical law that is based on theory and experimentation and used to describe the physics of a collision between bodies. Many impact law models have been developed, some of which include friction [7, 8, 11, 21, 28, 40, 18] and some which do not [9, 10]. Impact laws can be split into two main classes, those suitable for *compliant* rigid bodies and those suitable for *non-compliant* rigid bodies. The first class of impact laws allows for deformation of the contacting regions of the bodies [5], whereas the second class of impact laws requires perfect rigidity together with some rigidity constraint [8].

The impact law used in this paper will be for non-compliant rigid-body impacts with friction. Typically, the main assumptions for non-compliant impacts are: (i) there is no deformation of the contact regions, (ii) an impact occurs at an isolated contact point, (iii) there is no moment impulse during impact, (iv) the contact duration is infinitesimal, (v) there is no change in generalised coordinates throughout the impact phase and (vi) the finite active forces can be neglected during impact, [8, 19].

The dynamics of rigid-body systems with impacts and friction is usually found by numerical integration of systems of ordinary differential equations (ODEs) corresponding to the mechanical system under question. There are two main schemes for how this is usually done, namely, *time-stepping* and *event-driven* schemes. How to choose one over the other depends on the class or type of mechanical system that is being analysed, how the impact law is resolved, and the type of numerical analysis one would like to perform. Time-stepping schemes consist of a time discretisation of the dynamics in which each time step is advanced by solving an appropriate *complementarity problem* [1]. In these schemes the moment of each collision or when changes in relative velocity between bodies occurs is not exactly located but instead some level of penetration can occur. This is the price to pay for using rigidly formulated time-stepping methods. These schemes are however very advantageous for the simulation of systems with a large number of degrees of freedom with multiple contacts, for example flows in a granular material or masonry structures. Event-driven schemes are also basically time-stepping schemes but the time for which a trajectory reaches a constraint or *discontinuity surface* is located as precisely as possible to avoid penetration. This

39 class of schemes can in turn be divided into two separate categories, the complementarity methods and the *hybrid*  
40 methods. As the name suggests, in the complementarity method a complementarity problem is solved as the event  
41 is located, whereafter the standard time-stepping scheme continues as discussed above [1].

42 In the hybrid methods, which are the focus of this paper, the integration is terminated when an event is  
43 located and a discrete map is applied to describe how the state changes at the event. When the map is applied  
44 the time-stepping scheme is restarted with the post-event states as the initial conditions with a new set of ODEs  
45 that reflect the new circumstance. Hybrid methods have some obvious drawbacks but also some very important  
46 advantages that we will use in this paper. The main complication of hybrid methods is that, since each event has  
47 to be identified and resolved individually, the complexity of all different combinations of events and ODEs grows  
48 very quickly with the number of possible events. Another complication is that for each event a mapping has to be  
49 found that reflects, in the case of this paper, what the impact law dictates. These issues make hybrid schemes only  
50 feasible for systems with relatively few different discontinuity surfaces [2, 35, 36]. However, on the positive side it is  
51 worth raising at least four different points. First, since the events are not included in the time stepping only ODEs  
52 with smooth dynamics have to be integrated and it is thus possible to use a suitable high-order integrator with  
53 well-known convergence properties so that trajectories can be found with high accuracy. Second, since no events will  
54 be lost during simulation hybrid methods are useful for the brute-force bifurcation analysis and in particular when  
55 *discontinuity-induced bifurcations* (DIBs) are involved. An example of a DIB, and something that will be seen in  
56 this article, is a *grazing bifurcation*. A grazing bifurcation occurs when, under parameter variation, a trajectory of a  
57 periodic orbit makes tangential contact with the discontinuity surface, resulting in a change in the system dynamics  
58 [30, 15]. Third, hybrid methods make the stability analysis of periodic orbits relatively straight forward since it is  
59 possible to calculate *saltation matrices* that "glue" fundamental solution matrices together for trajectories passing  
60 through regions between different events. Fourth, despite the common misconception, there are methods born out  
61 of hybrid schemes for impacting systems that can deal with the accumulation of impacts, sometimes referred to  
62 as *chatter* or *Zeno* behaviour, and also calculate the corresponding saltation matrices [31]. As mentioned above,  
63 event-driven schemes are particularly useful for systems with relatively few degrees of freedom, but with multiple  
64 spatially and temporally separated contact points. Some examples include turbine blade dampers, friction clutch  
65 vibrations, landing gear dynamics [33], passive walkers [2, 34] and braille printers [13].

66 The use of nonsmooth system theory to predict and understand the kinematics of colliding rigid bodies in the  
67 presence of impact and friction is a useful commodity in engineering in particular and research of such systems  
68 in general [6, 16, 22, 25, 33, 37]. It is well known that nonsmooth systems can exhibit complex behaviour that  
69 cannot be found in smooth systems. The class of systems with combinations of ODEs and maps, that we use  
70 here for mechanical systems with impact and/or friction, are often termed as *piecewise-smooth* (PWS) systems. In  
71 recent years the interest of DIBs found in PWS systems have increased dramatically, and as mentioned above the  
72 main driver of the analysis of DIBs have been the hybrid system approach, where local behaviour can numerically  
73 be pinpointed with high accuracy [3, 12, 15, 30, 31]. In particular DIBs in impacting systems without friction  
74 have been studied extensively and some classification methodologies have been developed in [14, 27, 24], but also  
75 impacting systems with friction have been studied from a DIB point of view [23, 17, 28]. As already mentioned,  
76 a type of behaviour that is very specific to impacting systems with rigid body impacts is chatter, which is the  
77 phenomenon whereby a system goes through an infinite number of impacts in a finite time period. Previous works  
78 on chatter have considered both frictionless systems [9, 12, 31] and systems with impacts and friction [23, 28, 29].  
79 An interesting example of an engineering-based frictionless system is analysed in [26], where the problem of gear  
80 rattle (chatter) in Roots blower vacuum pumps is considered, and where the rattle is induced from the gear teeth  
81 losing and regaining contact. Similarly, in cam-follower systems for certain conditions the follower detaches from  
82 the cam, resulting in a series of unwanted impacts or chatter [3, 4, 32].

83 With this in mind, the emphasis of this paper is two-fold. First, we will show how the impact mappings for  
84 impacts with friction derived in [28] can be implemented for reliable simulations of systems with impacts and  
85 friction. Second, we want to exploit the fact that we have reliable simulation routines to analyse the long-term  
86 qualitative behavior of an unconstrained mechanical system with impacts and friction. Since previous research  
87 has mainly considered long-term dynamics for systems with impacts but without friction [3, 14, 31] the analysis of  
88 the unconstrained object will show that it is feasible to also consider long-term simulations for mechanical system  
89 with impact and friction. For this purpose we chose a hybrid event-driven technique as opposed to a time-stepping  
90 method in order to resolve DIBs in brute-force bifurcation analysis as well as deal with accumulation of events  
91 (chatter). We will use the example of a planar slender rod impacting with an oscillating surface to show how to  
92 implement these techniques. This can be seen as a generalisation of a system where a machine element detaches  
93 and is free to vibrate in the presence of friction or an item that lies on a vibrating conveyor belt. We will show  
94 how rattle is affected by the presence of friction.

95 This article is organised as follows. The equations of motion for a collision between two rigid bodies with an  
 96 isolated contact point are derived in Section 2.2 along with an extension of the energetic impact law derived in [28]  
 97 to allow for a two-body collision. Section 3 summarises the numerical methods necessary for the implementation of  
 98 the chosen impact law. In Section 3.1 we will introduce the notion of system states and how this idea is used in the  
 99 simulation of impacting systems. The model example of a slender rod impacting a periodically oscillating surface  
 100 is introduced in Section 4 and the basic setup that is used in the numerical simulations is presented in Section 4.1.  
 101 The paper concludes with a discussion in Section 5 that provides an insight for engineers and other researchers  
 102 working with impact and friction.

## 103 2. Planar rigid-body impacts with friction

104 In this section we will derive a general framework for a planar rigid-body collision between two unconstrained  
 105 objects. We will present an extension of the energetic impact mapping derived in [28], which will be used for the  
 106 model example in Section 4. The extension derived here is more general than the mapping presented in [28] in  
 107 that the mapping in [28] is for the specific case of a slender rod impacting a stationary non-compliant surface, but  
 108 where we allow both bodies to be unconstrained.

### 109 2.1. Equations of motion

110 Consider two planar rigid bodies  $H$  and  $H'$  whose configuration relative to an inertial reference frame can be  
 111 described in terms of vectors of generalized coordinates. Further impose that the bodies at any moment have a  
 112 finite number of isolated contact points and contact can not occur at two separate points simultaneously. For this  
 113 purpose we derive the equations of motion for two separate cases, when the bodies are in free flight, see Fig. 1  
 (a), and when they are in contact at an isolated point  $C$ , see Figs. 1 (b) and (c). The corresponding dynamics

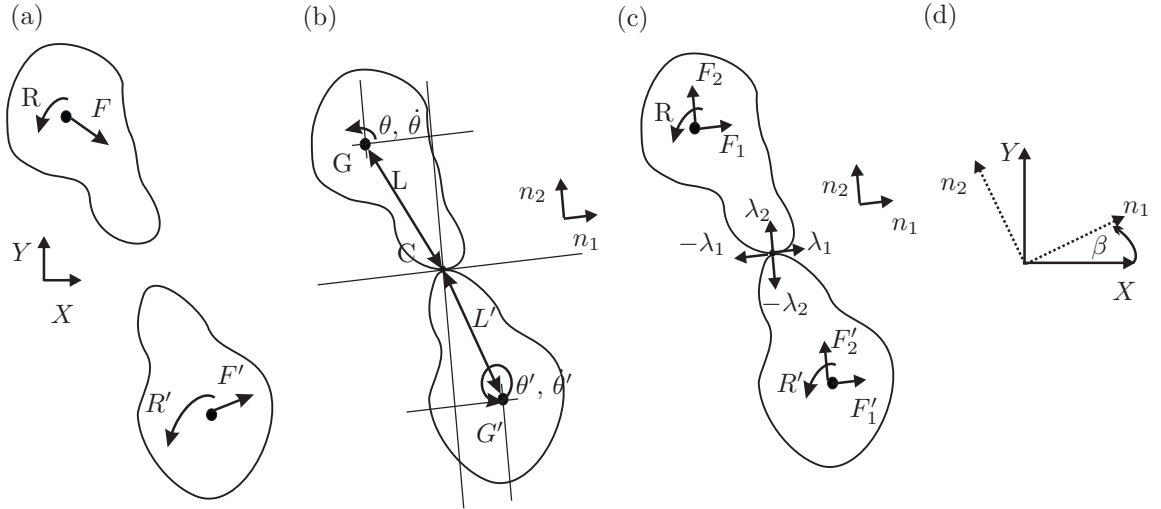


Figure 1: (a) A free-body force diagram for two planar bodies in free flight. (b) Geometry of two planar rigid bodies  $H$  and  $H'$  in contact at a point  $C$ . (c) A free-body force diagram corresponding to the figure in (b). (d) A schematic showing the angle of rotation  $\beta$  between the two frames used for modelling and analysis.

114 can be described using a Lagrangian formulation or using a Newtonian formulation. In Sections 2.1.1 and 2.1.2 we  
 115 consider a Newtonian formulation.  
 116

#### 117 2.1.1. Free flight

Consider the two bodies  $H$  and  $H'$  in free flight as shown in Fig. 1(a). The position and rotation of the centre of mass  $G$  of body  $H$  can be described in the  $X - Y$  plane by the coordinates  $q_X$  and  $q_Y$  and the angle  $\alpha$ , and similarly  $q'_X$  and  $q'_Y$  are the coordinates and  $\alpha'$  the rotation of the centre of mass  $G'$  of body  $H'$  (see Fig. 1(a)). Next we let

$$r = (q_X, q_Y, \alpha)^T, \quad r' = (q'_X, q'_Y, \alpha')^T,$$

$$\dot{r} = (\dot{q}_X, \dot{q}_Y, \dot{\alpha})^T, \quad \dot{r}' = (\dot{q}'_X, \dot{q}'_Y, \dot{\alpha}')^T,$$

$$\ddot{r} = (\ddot{q}_X, \ddot{q}_Y, \ddot{\alpha})^T \quad \text{and} \quad \ddot{r}' = (\ddot{q}'_X, \ddot{q}'_Y, \ddot{\alpha}')^T.$$

118 The equations of motion for the two bodies can now be written as

$$M\ddot{r} = F^T \quad \text{and} \quad M'\ddot{r}' = F'^T, \quad (1)$$

119 where  $M$  and  $M'$  are, respectively, the mass matrices for  $H$  and  $H'$  given by

$$M = \begin{pmatrix} m & 0 & 0 \\ 0 & m & 0 \\ 0 & 0 & I \end{pmatrix} \quad \text{and} \quad M' = \begin{pmatrix} m' & 0 & 0 \\ 0 & m' & 0 \\ 0 & 0 & I' \end{pmatrix},$$

120 and  $F$  and  $F'$  are, respectively, the external forces and torques acting on  $H$  and  $H'$  given by

$$F = (F_X, F_Y, R) \quad \text{and} \quad F' = (F'_X, F'_Y, R').$$

121 Here  $m$  and  $m'$  are the masses and  $I$  and  $I'$  are the moments of inertia of  $H$  and  $H'$ , respectively. Further  $F_X$ ,  $F'_X$   
122 and  $F_Y$ ,  $F'_Y$  represent the force components in the  $X - Y$  plane and  $R$  and  $R'$  are the external torques acting on  
123  $H$  and  $H'$ , respectively, as shown in Fig. 1(a).

### 124 2.1.2. Contact

Next we derive the equations of motion for the system when the two objects are in contact, as shown in Figs. 1(b) and (c). To do this we define a new coordinate system  $n_1 - n_2$ , rotated by an angle  $\beta$  about the origin relative to the coordinate system  $X - Y$ , where  $n_1$  is the tangential vector to the contact plane and  $n_2$  is the normal vector to the contact plane (see Fig. 1(d)). We also define  $\theta = \alpha - \beta$  and  $\theta' = \alpha' - \beta$  and let

$$q = (q_1, q_2, \theta)^T = (q_X \cos(\beta) - q_Y \sin(\beta), q_X \sin(\beta) + q_Y \cos(\beta), \alpha - \beta)^T,$$

and

$$q' = (q'_1, q'_2, \theta')^T = (q'_X \cos(\beta) - q'_Y \sin(\beta), q'_X \sin(\beta) + q'_Y \cos(\beta), \alpha' - \beta)^T.$$

125 Further, defining  $L$  as the distance from  $G$  to  $C$  and  $L'$  as the distance from  $G'$  to  $C$ , the positions  $q_C$  and  $q'_C$   
126 of the contact point  $C$  relative to both bodies in the  $n_1 - n_2$  frame can be written as

$$q_C := (q_1 - L \cos(\theta), q_2 - L \sin(\theta))^T \quad (2)$$

127 and

$$q'_C := (q'_1 - L' \cos(\theta'), q'_2 - L' \sin(\theta'))^T. \quad (3)$$

128 Note that we do not deal with the problem of finding the contact points in the general case but assume that there  
129 are well-defined contact points on each object. Let  $d = q_C - q'_C$  be the relative distance between the contact  
130 points of the two bodies. Then the unilateral constraint between the two bodies is  $d = (0, 0)^T$  or equivalently when  
131  $q_C = q'_C$ .

This is a useful framework to work with, particularly when deriving an impact mapping. It is also straightforward to translate back positions and angles to the original  $X - Y$  coordinate system. The derivation of the impact mapping introduced in [28] splits contact forces into tangential and normal components in relation to the contact plane, i.e. using the  $n_1 - n_2$  coordinate system. In order to relate how the contact forces will affect the centre of mass in terms of translations and rotations we need to consider

$$\frac{\partial q_C}{\partial q} = \begin{pmatrix} 1 & 0 & L \sin(\theta) \\ 0 & 1 & -L \cos(\theta) \end{pmatrix} \quad \text{and} \quad \frac{\partial q_C}{\partial q'} = \begin{pmatrix} 1 & 0 & L' \sin(\theta') \\ 0 & 1 & -L' \cos(\theta') \end{pmatrix}.$$

132 Now, the equations of motion for  $H$  and  $H'$  during contact can, respectively, be written as

$$M\ddot{q} = \hat{F}^T + \left( \frac{\partial q_C}{\partial q} \right)^T \lambda^T \quad (4)$$

133 and

$$M'\ddot{q}' = \hat{F}'^T + \left( \frac{\partial q_C}{\partial q'} \right)^T \lambda'^T, \quad (5)$$

134 where  $\hat{F}$  and  $\hat{F}'$  are, respectively, the external forces and torques acting on  $H$  and  $H'$  given by

$$\hat{F} = (F_1, F_2, R) = (F_X \cos(\beta) - F_Y \sin(\beta), F_X \sin(\beta) + F_Y \cos(\beta), R),$$

135 and

$$\hat{F}' = (F'_1, F'_2, R') = (F'_X \cos(\beta) - F'_Y \sin(\beta), F'_X \sin(\beta) + F'_Y \cos(\beta), R'),$$

136 where the subscripts 1 and 2, respectively, represent the components of the external forces acting in the tangential  
137 and normal direction, and  $R$  and  $R'$  are as above the external torques acting on the bodies as shown in Fig. 1 (c).  
138 In a similar way we define  $\lambda$  and  $\lambda'$  as the forces generated at impact of each body given by

$$\lambda = (\lambda_1, \lambda_2) \quad \text{and} \quad \lambda' = (-\lambda_1, -\lambda_2).$$

139 This setup is general and does not specify the mechanism that generates the tangential force  $\lambda_1$ . For this work  
140 however we assume that any tangential force arises due to friction at the contact point of the colliding bodies and  
141 here we use the Amontons-Coulomb friction law

$$\lambda_1 = \pm \mu \lambda_2 \tag{6}$$

142 for some non-negative constant  $\mu$  representing a coefficient of friction. The sign assigned to the tangential force  
143  $\lambda_1$  is positive (+) when the relative tangential contact point velocity between the two bodies is negative and it is  
144 negative (-) when the relative tangential contact point velocity is positive.

## 145 2.2. Energetic Impact Law

146 For collisions between rigid bodies, dissipation of energy in the direction normal to the contact plane is modelled  
147 using a coefficient of restitution. A coefficient of restitution gives a relation between the normal impulse applied  
148 during the restitution phase to that applied during compression. Typically a Newtonian coefficient or a kinematic  
149 coefficient is used for this purpose [38], however, for situations where the direction of slip can vary throughout  
150 the impact phase both these coefficients will violate energy conservation [39]. Stronge [38] views the impact phase  
151 as being composed of a compression phase followed by a restitution phase. During compression, kinetic energy is  
152 stored as internal deformation energy until the normal relative contact point velocity is brought to zero. At this  
153 point the restitution phase begins and the stored energy is released.

154 For this purpose Stronge defines an energetic coefficient of restitution  $e_*$  as follows:

155 **Definition 1.** *The square of the coefficient of restitution is the negative ratio of the elastic strain energy released*  
156 *during restitution to the internal energy of deformation absorbed during compression,*

$$e_*^2 = -\frac{W(P_f) - W(P_c)}{W(P_c)},$$

157 where  $W = \int_0^t F v dt'$  and for a significantly short contact duration the force can be related to the differential of  
158 impulse,  $dP = F dt'$  so that

$$e_*^2 = -\frac{\int_{P_c}^{P_f} v(P) dP}{\int_0^{P_c} v(P) dP}, \tag{7}$$

159 where  $P$  is the impulse,  $v(P)$  is the relative normal velocity,  $P_c = \int_0^{t_c} \lambda_N dt$  is the normal impulse for compression,  
160 with  $t_c$  the time taken for the contact point velocity to reach zero,  $\lambda_N$  the normal component of the contact force  
161 and  $P_f$  is the final impulse achieved at separation.

162 This energetic restitution coefficient allows for the various stick-slip processes that can occur throughout the  
163 impact phase and thus is a restitution coefficient that will not violate energy conservation. It is notable that the  
164 kinematic and Newtonian coefficients do not allow for situations where the direction of slip can vary throughout  
165 the impact phase, and the consequence of this is that the final impulse is not calculated correctly. Further, the  
166 energetic restitution coefficient forms the basis for the impact mapping derived in [28], a brief description of which  
167 will be given below. When we refer to the impact phase we are considering velocity changes which occur as a  
168 function of normal impulse. This impulse formulation is a natural framework to use given that we assume the  
169 impact is of infinitesimal contact duration.

170 In order to map pre-impact velocities to post-impact ones it is necessary to consider the terminal impulse  $P_f$   
171 for the given collision. Incorporating Amontons-Coulomb friction law (6) and the energetic restitution coefficient

172 (7) allows for a variety of stick-slip processes, each of which need to be considered and the corresponding  $P_f$  in  
 173 each case determined. We will consider the equations of motion for a planar two-body collision. It is necessary to  
 174 consider velocity changes as a function of normal impulse  $P$  instead of the time variable  $t$ . Consider (4) translated  
 175 to the contact point  $q_C$  so that

$$\frac{d\dot{q}_C}{dt} = \frac{\partial q_C}{\partial q} \ddot{q} = \frac{\partial q_C}{\partial q} M^{-1} \left( \frac{\partial q_C}{\partial q} \right)^T \lambda^T + \frac{\partial q_C}{\partial q} M^{-1} F^T = w^{-1} \lambda^T + f(F_1, F_2, R, q, \dot{q}) \quad (8)$$

176 and

$$\frac{d\dot{q}_C}{dt} = \frac{\partial q_C}{\partial q'} \ddot{q} = \frac{\partial q_C}{\partial q'} (M')^{-1} \left( \frac{\partial q_C}{\partial q'} \right)^T \lambda'^T + \frac{\partial q_C}{\partial q'} (M')^{-1} F'^T = (w')^{-1} \lambda'^T + f'(F'_1, F'_2, R', q', \dot{q}'), \quad (9)$$

which is the rate of change of the contact point velocities as a function of time and where  $w^{-1}$  and  $(w')^{-1}$  are the symmetric matrices given by

$$w^{-1} = \frac{\partial q_C}{\partial q} M^{-1} \left( \frac{\partial q_C}{\partial q} \right)^T = \begin{pmatrix} A & B \\ B & C \end{pmatrix},$$

$$(w')^{-1} = \frac{\partial q_C}{\partial q'} (M')^{-1} \left( \frac{\partial q_C}{\partial q'} \right)^T = \begin{pmatrix} A' & B' \\ B' & C' \end{pmatrix},$$

where

$$A = \frac{1}{m} + \frac{L^2 \sin^2(\theta)}{I}, \quad B = \frac{-\sin(\theta) \cos(\theta)}{I}, \quad C = \frac{1}{m} + \frac{L^2 \cos^2(\theta)}{I}$$

$$A' = \frac{1}{m'} + \frac{L'^2 \sin^2(\theta')}{I'}, \quad B' = \frac{-\sin(\theta') \cos(\theta')}{I'}, \quad C' = \frac{1}{m'} + \frac{L'^2 \cos^2(\theta')}{I'}.$$

177 In this context we do not need to consider terms which do not change throughout the impact phase and therefore  
 178 we can neglect the functions  $f$  and  $f'$ . Further, during the impact phase we also have that

$$\frac{dP}{dt} = \lambda_2 \quad (10)$$

179 for  $H$  and by Newton's third law of motion

$$\frac{d(-P)}{dt} = -\lambda_2 \quad (11)$$

180 for  $H'$ , since the normal impulse is a uniformly increasing scalar function during contact. Now, (8), (10) and (11)  
 181 allow us to replace the independent variable  $t$  with  $P$  in (10) and (11) to give

$$\frac{d\dot{q}_C}{dP} = \frac{1}{\lambda_2} w^{-1} \begin{pmatrix} \lambda_1 \\ \lambda_2 \end{pmatrix}, \quad (12)$$

182 which is the rate of change of contact point velocities with respect to  $H$  as a function of normal impulse. In a  
 183 similar way, using (9), (10) and (11), we also have

$$\frac{d\dot{q}'_C}{dP} = \frac{1}{\lambda_2} (w')^{-1} \begin{pmatrix} -\lambda_1 \\ -\lambda_2 \end{pmatrix}. \quad (13)$$

184 Subtracting (13) from (12) yields

$$\frac{d\dot{\tilde{q}}_C}{dP} := \frac{d\dot{q}_C}{dP} - \frac{d\dot{q}'_C}{dP} = \frac{1}{\lambda_2} \left( w^{-1} + (w')^{-1} \right) \begin{pmatrix} \lambda_1 \\ \lambda_2 \end{pmatrix}, \quad (14)$$

185 or in the notation of [28]

$$\frac{d\dot{\tilde{q}}_C}{dP} = \frac{1}{\lambda_2} \begin{pmatrix} \hat{A} & -\hat{B} \\ -\hat{B} & \hat{C} \end{pmatrix} \begin{pmatrix} \lambda_1 \\ \lambda_2 \end{pmatrix}, \quad (15)$$

186 which is the relative change in contact point velocities as a function of normal impulse. Expanding Eq. (15) and  
 187 writing it in terms of tangential and normal components, respectively, gives

$$\frac{d\dot{\tilde{q}}_{1C}}{dP} = \hat{A} \frac{\lambda_1}{\lambda_2} - \hat{B}, \quad \frac{d\dot{\tilde{q}}_{2C}}{dP} = -\hat{B} \frac{\lambda_1}{\lambda_2} + \hat{C}, \quad (16)$$

188 which will be used to define the rate constants used for the impact mappings presented below.

189 Stronge [38] describes four possible impact-phase processes and calculates the terminal impulse and the post-  
 190 impact velocity components for each phase. The four phases are:

191 **Unidirectional slip during contact.** In this case slip does not cease throughout the impact phase, and the  
 192 tangential forcing acts in a direction opposite to the motion of the body.

193 **Slip reversal during compression.** In this situation initial sliding is brought to rest and then reverses direction.

194 **Slip-stick transition during compression.** The case whereby initial sliding is brought to rest. The contact  
 195 point sticks if the friction coefficient  $\mu$  is sufficiently large or undergoes reverse slip if it is not. It is also  
 196 required that the initial sliding velocity is sufficiently small, otherwise this motion can not occur.

197 **Jam.** This is the process whereby there is an increase in normal acceleration at the contact point due to a large  
 198 rotational acceleration. This motion occurs during an initial period of sliding.

199 Nordmark *et al.* [28] extend this theory by describing 10 different impact regions from which an impact law  
 200 consisting of three mappings is derived. The impact mappings in [28] map the relative tangential and normal  
 201 contact point velocities before the impact phase  $\hat{q}_C^-$  to the post-impact phase velocities  $\hat{q}_C^+$ . Using Eq. (16) and  
 202 following [28] we define the rate constants  $k_T^+$ ,  $k_T^-$ ,  $k_N^+$ ,  $k_N^-$ ,  $k_T^0$  and  $k_N^0$ . These rate constants describe how stick and  
 203 positive and negative slip can occur throughout the compression and restitution phase. For the various stick-slip  
 204 processes described above Nordmark *et al.* [28] define the rate constants

$$\begin{aligned} k_T^+ &= -\hat{B} - \mu\hat{A}, & k_N^+ &= \hat{C} + \mu\hat{B}, \\ k_T^- &= -\hat{B} + \mu\hat{A}, & k_N^- &= \hat{C} - \mu\hat{B}, \\ k_T^0 &= 0, & k_N^0 &= \frac{\hat{A}\hat{C} - \hat{B}^2}{\hat{A}}, \end{aligned}$$

205 from which

$$k_T = \begin{cases} k_T^+, & \text{in positive slip,} \\ k_T^-, & \text{in negative slip,} \\ k_T^0, & \text{in stick,} \end{cases} \quad (17)$$

206 and

$$k_N = \begin{cases} k_N^+, & \text{in positive slip,} \\ k_N^-, & \text{in negative slip,} \\ k_N^0, & \text{in stick,} \end{cases} \quad (18)$$

209 can be determined, where  $\mu = \frac{\lambda_1}{\lambda_2}$ . It is worth mentioning that  $\mu$  is taken as an absolute here and the rate constants  
 210 described above consider all cases of positive and negative slip so it is not necessary to assign a sign to  $\mu$ . Nordmark  
 211 *et al.* [28] also define the constants  $k'_T$  and  $k'_N$ , which are assigned one of the values of  $k_T^+$ ,  $k_T^-$ ,  $k_N^+$ ,  $k_N^-$ ,  $k_T^0$  and  $k_N^0$ ,  
 212 and determined by the system parameters and pre-collision conditions. For full details we refer to [28]. From this  
 213 and using Eq. (7) the following three maps, for pre-impact to post-impact contact point velocities  $\hat{q}_C^- \mapsto \hat{q}_C^+$  can be  
 214 derived:

215 **Map I:**

$$\hat{q}_{1C}^+ = \hat{q}_{1C}^- - (1 + e_*) \frac{k_T}{k_N} \hat{q}_{2C}^- \quad (19)$$

$$\hat{q}_{2C}^+ = -e_* \hat{q}_{2C}^- \quad (20)$$

217 **Map II:**

$$\hat{q}_{1C}^+ = \frac{k'_T}{k'_N} \left( \frac{k_N}{k_T} \hat{q}_{1C}^- - \hat{q}_{2C}^- + \sqrt{\left(1 - \frac{k'_N}{k_N}\right) \left(\frac{k_N}{k_T} \hat{q}_{1C}^- - \hat{q}_{2C}^-\right)^2 + e_*^2 \frac{k'_N}{k_N} (\hat{q}_{2C}^-)^2} \right) \quad (21)$$

$$\hat{q}_{2C}^+ = \sqrt{\left(1 - \frac{k'_N}{k_N}\right) \left(\frac{k_N}{k_T} \hat{q}_{1C}^- - \hat{q}_{2C}^-\right)^2 + e_*^2 \frac{k'_N}{k_N} (\hat{q}_{2C}^-)^2} \quad (22)$$

$$\dot{q}_{1C}^+ = \frac{k'_T}{k'_N} \left( \frac{k_N}{k_T} \dot{q}_{1C}^- - \dot{q}_{2C}^- + e_* \sqrt{\left(1 - \frac{k'_N}{k_N}\right) \left(\frac{k_N}{k_T} \dot{q}_{1C}^- - \dot{q}_{2C}^-\right)^2 + e_*^2 \frac{k'_N}{k_N} (\dot{q}_{2C}^-)^2} \right) \quad (23)$$

$$\dot{q}_{2C}^+ = e_* \sqrt{\left(1 - \frac{k'_N}{k_N}\right) \left(\frac{k_N}{k_T} \dot{q}_{1C}^- - \dot{q}_{2C}^-\right)^2 + \frac{k'_N}{k_N} (\dot{q}_{2C}^-)^2} \quad (24)$$

221 for  $k_N \neq 0$  and

$$\dot{q}_{1C}^+ = 0 \quad (25)$$

$$\dot{q}_{2C}^+ = e_* \sqrt{(\dot{q}_{2C}^-)^2 + \frac{2k'_N \dot{q}_{1C}^- \dot{q}_{2C}^-}{k_T}} \quad (26)$$

222 for  $k_N = 0$ .

223 As mentioned above, the different combinations of segments of stick and relative slip can be described by ten  
 224 different regions, each of which corresponds to one of the three maps given above. It is worth noting that in [40] an  
 225 equivalent energetic coefficient of restitution is used together with the Amontons-Coulomb friction law to describe  
 226 the contact and impact dynamics for the case of a bouncing dimer.

### 227 2.3. Dynamics

228 As the type of mechanical system considered for this work is unconstrained away from the discontinuity surfaces,  
 229 various possible modes of sustained motion can occur. To highlight this, in Fig. 2 we consider a schematic of the  
 230 time history of a point  $p(t)$  on a rigid body that occasionally acts as a contact point during impacts with a non-  
 compliant surface. We only need to define three modes of motion, namely, unconstrained free flight, chatter and

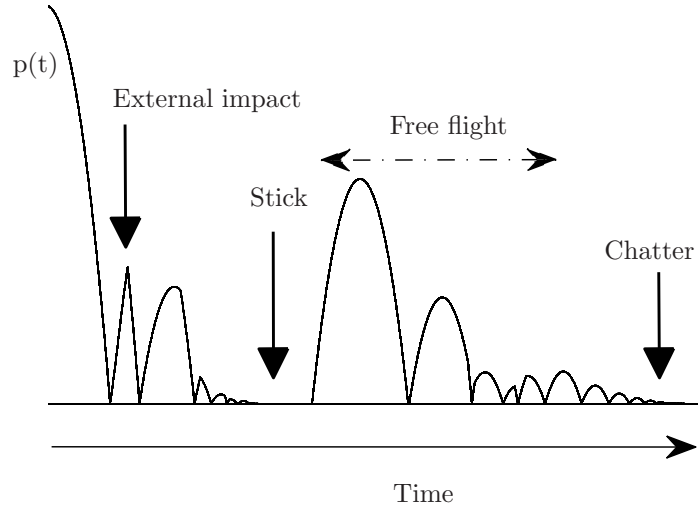


Figure 2: A schematic detailing the time history of a contact point  $p(t)$  in an impacting system.

232 stick. For our purposes, unconstrained free flight could describe, for example, the motion of a projectile that is free  
 233 to rotate about all axes and is entirely unconstrained. Note that constrained free flight could describe, for example,  
 234 the motion of a double pendulum. The system is constrained to move in a plane with two degrees of freedom due  
 235 to the upper arm of the pendulum being constrained to a fixed point. It is also necessary to distinguish between  
 236 two types of chatter, namely, complete and incomplete chatter [31]. Complete chatter is where an object undergoes  
 237 an infinite number of impacts in finite time and eventually transitions to stick. This motion can be observed in

238 reality where a bouncing ball, for example, undergoes a large number of impacts and eventually comes to a stop  
239 and transitions into a stick state. Incomplete chatter is where the system undergoes a large number of impacts in  
240 a short time frame but transitions to free flight due to a change in the relative acceleration.

241 At an impact, after free flight, a system can evolve in a number of different ways: It can continue in free flight  
242 motion, go into a stick regime or go through a chatter sequence. A feature which is also present in the schematic  
243 Fig. 2 is an *External impact*, where another point of the rigid-body system impacts and thus causes a change in  
244 the dynamics of the point  $p(t)$ . For analysis purposes it is important to be able to distinguish between the different  
245 features and subtle changes in order to understand the mechanisms that cause them. There are typically also a  
246 number of system-specific long-term dynamical behaviours present. In Section 4.1 and 4.3 we discuss such examples  
247 for the case of a slender rod impacting an oscillating surface.

### 248 3. Numerical methods

249 In this section we will give a very brief description of the different numerical methods employed for simulation  
250 of the rigid-body system with impacts and friction described in Section 4. We mainly follow the methodologies  
251 described in [31] and [36] with some extensions and some simplifications, as we will describe below. The methodology  
252 we use here is, as mentioned in Section 1, sometimes referred to as the hybrid or event-driven approach, where  
253 continuous dynamics, described by a system of smooth ODEs, is combined with discrete events, described by  
254 maps. The maps are used when a solution trajectory reaches an *event surface* defined by the system variables  
255 and parameters. In this context we consider the continuous dynamics as the motion between the impacts or other  
256 transitions and the maps correspond to the actual impacts or transitions. The transitions are typically changes  
257 from free-flight dynamics to stick or to chatter.

258 To solve a system of smooth ODEs in Section 4 we mainly use the MATLAB's ODE solver `ode45` and to locate  
259 the event surfaces we use MATLAB's built-in event-detection routines. However, the methodology described here  
260 can equally well be implemented in any environment that has an ODE solver and event location capabilities. The  
261 ODE solver requires at least two vector fields (one for the free-flight phase and one for stick, but see further Section  
262 4 for a specific implementation), simulation times, initial conditions, error tolerances and integration step sizes.  
263 In order to accurately locate the event surfaces, event functions need to be described that are derived from the  
264 geometries of the impacting rigid bodies. Finally, impact maps, like those described in Section 2.2 have to be  
265 defined together with a process that determines what impact map to use for the specific impact.

266 In general, when dealing with rigid bodies, it is more than likely that the overall system can have multiple  
267 contact points and a large number of events can occur (impacts or vector field transitions). These two factors can  
268 generally give rise to a number of computational complications, making the analysis of long-term dynamics difficult.  
269 One such useful example is to define an additional artificial term on the vector fields that makes the surface locally  
270 attractive when the system is in stick. This ensures that the contact point does not drift away from the surface  
271 due to numerical errors. A similar approach was used in [36] for Filippov systems.

272 Following the setup of system states presented in [36, 31] we can achieve a robust numerical code capable of  
273 simulating the system to examine long-term dynamics. By robust we mean, using this method, the numerical  
274 simulator is capable of handling the events and transitions which can occur, without breaking down. This is  
275 presented in Section 3.1, followed by a discussion in Section 3.2 on brute-force bifurcation analysis in general and  
276 stability analysis of symmetric period-1 solutions.

#### 277 3.1. System States

278 One of the many difficulties associated with using a hybrid strategy for finding the solution to a dynamical  
279 system with discontinuities is the accumulation of events, for instance when an incomplete or a complete chattering  
280 sequence is encountered (see Section 2.3 and [4]). To deal with this in a systematic manner it is advantageous to  
281 introduce the notion of system states in a similar way as was done in [36, 31]. For a general system we can define  $n$   
282 discrete states  $S_n$  in which one of the defined vector fields  $\Phi_n$  is being used. Each vector field  $\Phi_n$  either corresponds  
283 to free-flight or sticking motion, which has to be defined by the user. A transition diagram can be used to decide if  
284 a system should transition from one state to another at an event, and also provides a means for numerically dealing  
285 with a complete chatter sequence.

286 The number of free-flight and stick states depends mainly on the geometry of the impacting rigid bodies. This  
287 point will be illustrated further in Section 4.2 for a model example showing a slender rod impacting an oscillating  
288 plane.

289 The mechanism for switching between the states  $S_n$  at impact involves evaluating relative normal contact point  
290 accelerations and velocities, whereafter a transition diagram together with a decision tree can be used to evaluate

291 what state the system should be in after the impact. The contact point velocities are mainly used to calculate  
 292 post-impact velocities. This is in contrast to the contact point accelerations that are used to determine when the  
 293 system should release from stick to free flight. The specific implementations have to be assessed on a case-by-case  
 294 basis.

### 295 3.2. Bifurcation diagrams and stability analysis

296 A common way in which to make an initial assessment of the long-term dynamics of a mechanical system is to  
 297 plot brute-force bifurcation diagrams. In Section 4.3 we highlight some aspects of how the long-term dynamics of  
 298 a mechanical system with impacts is affected by friction through bifurcation diagrams. The bifurcation diagrams  
 299 shown in Section 4.3 are made up of, on the one hand, period-1 solutions found by a semi-analytic continuation  
 300 method based on a shooting method and, on the other hand, other recurrent motions found by brute-force simulation  
 301 methods. For the period-1 solutions the stabilities are found by calculating the eigenvalues of the fundamental  
 302 solution matrix that is found by solving the variational equations of the piecewise-smooth system. For this purpose  
 303 saltation matrices are used to merge together fundamental solution matrices for trajectories that switch from one  
 304 state to another. These methods have successfully been implemented in [2, 13, 34] and particularly in [31] which  
 305 reports the stability analysis for impacting systems without friction but with complete chatter.

## 306 4. Dynamics of a slender rod impacting a periodically-oscillating surface

307 In this section we will use a basic planar model of a rigid slender rod impacting a periodically oscillating surface  
 308 to illustrate the techniques discussed in Section 2. The model will also be used to describe how the numerical  
 309 methods discussed in Section 3 can be implemented and what the dynamical features presented in Section 2.3 look  
 310 like for this specific case. We will also use this setup to show how friction affects chaotic rattling behaviour of the  
 311 rod.

### 312 4.1. The model, system states and vector fields

313 As discussed above we consider a planar uniform slender rigid rod and let  $q_1, q_2$  be the tangential and normal  
 314 position of the centre of mass, relative to the contact plane, and let  $\theta$  be the angle of rotation of the rod (see  
 315 Fig. 3(a)). For this model example the tangential and normal direction correspond to the  $n_1$  and  $n_2$  directions,  
 316 respectively, as discussed in Section 2 and shown in Fig. 1. The rod is subjected to gravity and where either of  
 317 the two isolated end points, named  $P_1$  and  $P_2$ , can impact, get stuck to or slide along the periodically oscillating  
 318 surface. The slender rod can essentially be in four different states: free flight (Fig. 3(a)), one of the two end points  
 319 is stuck to the surface (Fig. 3(b) and (c)), or both end points are stuck to the surface (Fig. 3(d)). The fourth state  
 320 here also allows for the release of the two end points at the same time, which in effect leads to a lower-dimensional  
 dynamical system that can be treated as a simple impacting particle.

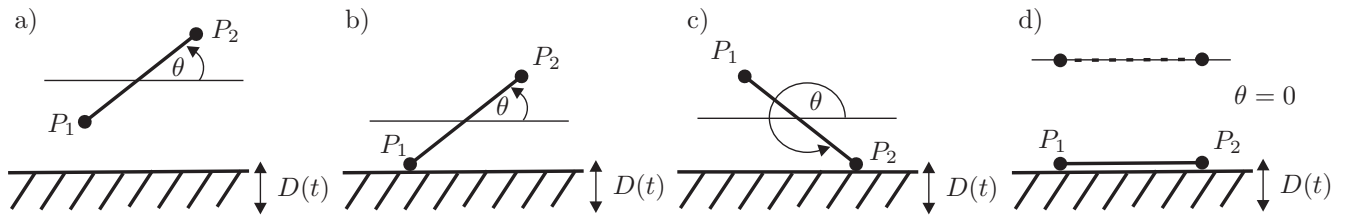


Figure 3: The four possible main states of the slender rod. (a) Free-flight motion. (b) End point  $P_1$  constrained to the surface. (c) End point  $P_2$  constrained to the surface. (d) Symmetric free-flight motion (dashed) and symmetric stick motion (solid).

321 Without loss of generality and following the general setup in Section 2, we let the mass of the rod be  $m = 1$  and  
 322 the distance from the centre of mass to either of the two end points be  $L = 1$ . This gives the moment of inertia  
 323  $I = \frac{1}{3}$  and the radius of gyration  $k_r^2 = \frac{1}{3}$ . We further assume that the vertically oscillating surface is not affected  
 324 by the rod at impact and thus let  $D(t)$  represent the oscillating surface with frequency  $\omega$ , amplitude  $A$  and where  $t$   
 325 is time, so that  $D(t) := A \sin(\omega t)$  (see Fig. 3). This means that we only need to consider one of the two impacting  
 326 bodies introduced in Section 2.1.1 as the mass of the surface can be assumed to be much greater than that of the  
 327 rod and thus only one of the two systems of differential equations, say Eq. (4), needs to be considered. For future  
 328 reference we let  $q_4 = \dot{q}_1, q_5 = \dot{q}_2, q_6 = \dot{\theta}$  and introduce  $\tau$  as the phase of the oscillating floor. We also let  $d_1$  be  
 329 the distance between the end point  $P_1$  and the surface in the normal direction and let  $d_2$  be the distance between the  
 330

331 end point  $P_2$  and the surface in the normal direction. The unilateral constraints for this model example are thus  
 332  $d_1 = 0$  (see Fig. 3 (b)), or  $d_2 = 0$  (see Fig. 3 (c)) or simultaneously  $d_1, d_2 = 0$  (see Fig. 3 (d)). Further, using Eq. (2)  
 333 we find

$$d_1 = q_2 - \sin(\theta) - A \sin(\omega t), \quad (27)$$

$$d_2 = q_2 + \sin(\theta) - A \sin(\omega t),$$

335 from which we obtain the relative velocity between the end point  $P_1$  and the floor as

$$\dot{d}_1 = \dot{q}_2 - \cos(\theta)\dot{\theta} - A\omega \cos(\omega t), \quad (28)$$

336 and the relative velocity between the end point  $P_2$  and the floor as

$$\dot{d}_2 = \dot{q}_2 + \cos(\theta)\dot{\theta} - A\omega \cos(\omega t),$$

337 the relative acceleration between the end point  $P_1$  and the floor as

$$\ddot{d}_1 = \ddot{q}_2 + \sin(\theta)\dot{\theta}^2 - \cos(\theta)\ddot{\theta} + A\omega^2 \sin(\omega t), \quad (29)$$

338 and the relative acceleration between the end point  $P_2$  and the floor as

$$\ddot{d}_2 = \ddot{q}_2 - \sin(\theta)\dot{\theta}^2 + \cos(\theta)\ddot{\theta} + A\omega^2 \sin(\omega t).$$

339 Now, we are ready to introduce the five system states, which we will use for simulating this mathematical model  
 340 of the planar rod, together with the corresponding vector fields.

341 **State 1 – Free flight.** Since we make the assumption that there is no external torque or no horizontally acting  
 342 forcing present, we have that  $R = 0$  and  $F_1 = 0$  in Eq. (4). The only external force acting in the vertical direction  
 343 is due to gravity, and so  $F_2 = -g$ . Following this, the equations of motion of the rod in free flight is given by

$$\ddot{q}_1 = 0, \quad (30)$$

$$\ddot{q}_2 = -g, \quad (31)$$

$$\ddot{\theta} = 0, \quad (32)$$

and the corresponding dynamical system is

$$(\dot{q}_1, \dot{q}_2, \dot{\theta}, \dot{q}_4, \dot{q}_5, \dot{q}_6, \dot{\tau})^T = (q_4, q_5, q_6, 0, -g, 0, 1)^T := \Phi_1(t)$$

344 that will be used for the numerical simulation of the free-flight motion. Notice that we have included the phase  $\tau$   
 345 in the dynamical system in order to have better control of the periodic influence of time.

346 **State 2 – End point  $P_1$  is stuck to the floor.** We will derive a new vector field for the system when  $P_1$  is  
 347 stuck to the floor. First, from Eq. (4) we get that the equations of motion for the constrained bar is

$$\ddot{q}_1 = \lambda_1, \quad (33)$$

$$\ddot{q}_2 = -g + \lambda_2, \quad (34)$$

$$\ddot{\theta} = 3 \sin(\theta)\lambda_1 - 3 \cos(\theta)\lambda_2. \quad (35)$$

348 Next, we need to find the forces  $\lambda_1$  and  $\lambda_2$  needed to constrain  $P_1$  to the oscillating surface. Substituting Eq. (34)  
 349 and Eq. (35) into Eq. (29) and using the Amontons-Coulomb friction law  $\lambda_1 = s\mu\lambda_2$  gives

$$\ddot{d}_1 = -g + \lambda_2 + \sin(\theta)\dot{\theta}^2 - 3 \cos \theta \sin(\theta)s\mu\lambda_2 + 3 \cos^2(\theta)\lambda_2 + A\omega^2 \sin(\omega t), \quad (36)$$

350 where  $s$  is either  $+1$  or  $-1$ , depending on the relative tangential velocity at impact. Further, using the fact that  
 351  $d_1 = \dot{d}_1 = \ddot{d}_1 = 0$  when the end point  $P_1$  is in contact with the surface and solving for  $\lambda_2$  gives

$$\lambda_2 = \frac{g - \sin(\theta)\dot{\theta}^2 - A\omega^2 \sin(\omega t)}{1 + 3 \cos^2(\theta) - 3s \cos(\theta) \sin(\theta)\mu}, \quad (37)$$

352 which is the normal forcing required to ensure that the contact point will remain constrained to the plane.

Last, we can write the vector field for the rod with the end point  $P_1$  stuck to the floor as

$$(\dot{q}_1, \dot{q}_2, \dot{\theta}, \dot{q}_4, \dot{q}_5, \dot{q}_6, \dot{\tau})^T = (q_4, q_5, q_6, \alpha_1, \alpha_2, \alpha_3, 1)^T := \Phi_2(t)$$

353 where

$$\begin{aligned}
\alpha_1 &= \frac{s\mu \left( g - \sin(\theta)\dot{\theta}^2 - A\omega^2 \sin(\omega t) \right)}{1 + 3 \cos^2(\theta) - 3s\mu \cos(\theta) \sin(\theta)}, \\
\alpha_2 &= -g + \frac{g - \sin(\theta)\dot{\theta}^2 - A\omega^2 \sin(\omega t)}{1 + 3 \cos^2(\theta) - 3s\mu \cos(\theta) \sin(\theta)}, \\
\alpha_3 &= \frac{(3s\mu \sin(\theta) - 3 \cos(\theta)) \left( g - \sin(\theta)\dot{\theta}^2 - A\omega^2 \sin(\omega t) \right)}{1 + 3 \cos^2(\theta) - 3s\mu \cos(\theta) \sin(\theta)}.
\end{aligned}$$

**State 3 – End point  $P_2$  is stuck to the floor.** Similarly, using symmetry, we can write the vector field for the rod with the end point  $P_2$  stuck to the floor as

$$(\dot{q}_1, \dot{q}_2, \dot{\theta}, \dot{q}_4, \dot{q}_5, \dot{q}_6, \dot{\tau})^T = (q_4, q_5, q_6, \alpha_4, \alpha_5, \alpha_6, 1)^T := \Phi_3(t)$$

354 where

$$\begin{aligned}
\alpha_4 &= \frac{s\mu \left( -g + \sin(\theta)\dot{\theta}^2 - A\omega^2 \sin(\omega t) \right)}{3s\mu \cos \theta \sin(\theta) - 1 - 3 \cos^2(\theta)}, \\
\alpha_5 &= -g + \frac{-g + \sin(\theta)\dot{\theta}^2 - A\omega^2 \sin(\omega t)}{3s\mu \cos \theta \sin(\theta) - 1 - 3 \cos^2(\theta)}, \\
\alpha_6 &= \frac{(3s\mu \sin(\theta) - 3 \cos(\theta)) \left( -g + \sin(\theta)\dot{\theta}^2 - A\omega^2 \sin(\omega t) \right)}{3s\mu \cos \theta \sin(\theta) - 1 - 3 \cos^2(\theta)}.
\end{aligned}$$

355 **State 4 – Symmetric motion.** We define symmetric motion as one where  $\theta \bmod \pi = q_6 = 0$  for all time, which  
356 means that the two end points will impact the floor at the same time. The dynamical system will be the same as  
357 in the free-flight case albeit the motion is heavily constrained, and thus the vector field  $\Phi_1$  can be used.

**State 5 – Both end points  $P_1$  and  $P_2$  stuck to the floor.** If both end points are stuck to the floor it means that the centre of mass will oscillate as  $D(\tau)$  and thus the vector field in this case is trivially

$$(\dot{q}_1, \dot{q}_2, \dot{\theta}, \dot{q}_4, \dot{q}_5, \dot{q}_6, \dot{\tau})^T = (q_4, q_5, q_6, 0, -\omega^2 A \sin(\omega \tau), 0, 1)^T := \Phi_4.$$

#### 358 4.2. State transitions and impact mappings

359 For the planar rod model described above in Section 4.1 we introduced five system states, two for free flight  
360 and three for stick. Our proposed scheme for dealing with chatter involves constraining the respective end point  
361 to the impact surface when that corresponding end point is going through a chatter sequence. The system then  
362 acts as a sliding hinge. For this purpose we define the critical normal contact point relative velocity as  $V_{tol}$  and  
363 use this, along with the end point accelerations, as criteria for deciding when the system is going through a chatter  
364 sequence.  $V_{tol}$  is chosen based on the system in question and what makes physical sense. In this paper we typically  
365 let  $V_{tol}$  be  $\leq 10^{-6}$ . When an impact occurs the critical normal contact point relative velocities  $\dot{d}_1$  and  $\dot{d}_2$  together  
366 with the critical normal contact point relative accelerations  $\ddot{d}_1$  and  $\ddot{d}_2$  are evaluated. These values are then used  
367 with a decision tree to decide if the system should transition to another state. It is important to note that when  
368 calculating the relative contact point accelerations when in a stick state, we use the unconstrained values. This  
369 approach ensures that the system will naturally release from stick due to the change in relative acceleration. At  
370 impact the impact law needs to be applied to determine what type of transition should occur. For the model  
371 example described here the rate constants defined in Section 2.2 now take the form

$$k_T^+ = -3 \sin(\theta) \cos(\theta) - \mu (1 + 3 \sin^2(\theta)), \quad k_N^+ = 1 + 3 \cos^2(\theta) + 3\mu \sin(\theta) \cos(\theta)$$

372 for positive slip,

$$k_T^- = -3 \sin(\theta) \cos(\theta) + \mu (1 + 3 \sin^2(\theta)), \quad k_N^- = 1 + 3 \cos^2(\theta) - 3\mu \sin(\theta) \cos(\theta)$$

373 for negative slip, and

$$k_{T0} = 0, \quad k_{N0} = \frac{4}{1 + 3 \sin^2(\theta)}$$

374 for the stick regime. These rate constants are used in the mappings for the numerical implementation together  
375 with a decision tree. The process involves deciding what region the impact corresponds to depending on initial  
376 conditions and assigning the corresponding rate constants and impact map accordingly, see further [28]. However,  
377 apart from deciding what will happen at a specific impact the system can also switch between the different states  
378 described in Section 4.1. The transition diagram describing what transitions are possible for the rod system are  
given in Fig. 4, where  $S_1 - S_5$  are the states introduced in Section 4.1.

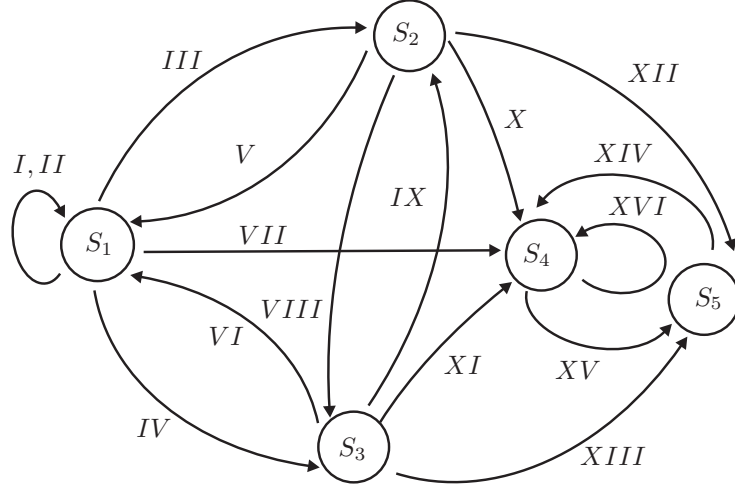


Figure 4: A transitions diagram for the planar rod system showing the five states,  $S_1 - S_5$  and the state transitions  $I - XVI$ . See also Table 1 for a list of event types and transition criteria.

379

Transition	Type	Event	Transition Criteria	Contact angle $\theta$	State
I	I	$d_1 = 0$	$ \dot{d}_1  > V_{tol}$ ,	$\neq 0$	$S_1 \rightarrow S_1$
II	I	$d_2 = 0$	$ \dot{d}_2  > V_{tol}$	$\neq 0$	$S_1 \rightarrow S_1$
III	C	$d_1 = 0$	$ \dot{d}_1  < V_{tol}$ ,	$\neq 0$	$S_1 \rightarrow S_2$
IV	C	$d_2 = 0$	$ \dot{d}_2  < V_{tol}$	$\neq 0$	$S_1 \rightarrow S_3$
V	R	$\ddot{d}_1 > 0$		$\neq 0$	$S_2 \rightarrow S_1$
VI	R	$\ddot{d}_2 > 0$		$\neq 0$	$S_3 \rightarrow S_1$
VII	L	$d_1 = 0, d_2 = 0$	$ \dot{d}_{1,2}  > V_{tol}, \theta \bmod \pi < \theta_{Crit}$	0	$S_1 \rightarrow S_4$
VIII	TR	$\ddot{d}_2 > 0$		0	$S_2 \rightarrow S_3$
IX	TR	$\ddot{d}_1 < 0$		0	$S_3 \rightarrow S_2$
X	T	$d_2 = 0$	$ \dot{d}_2  > V_{tol}$	0	$S_2 \rightarrow S_4$
XI	T	$d_1 = 0$	$ \dot{d}_1  > V_{tol}$	0	$S_3 \rightarrow S_4$
XII	TC	$d_2 = 0$	$ \dot{d}_2  < V_{tol}$	0	$S_2 \rightarrow S_5$
XIII	TC	$d_1 = 0$	$ \dot{d}_1  < V_{tol}$	0	$S_3 \rightarrow S_5$
XIV	R	$\ddot{d}_{1,2} > g$		0	$S_5 \rightarrow S_4$
XV	TC	$d_1 = 0, d_2 = 0$	$ \dot{d}_1  < V_{tol},  \dot{d}_2  < V_{tol}$	0	$S_4 \rightarrow S_5$
XVI	T	$d_1 = 0, d_2 = 0$	$ \dot{d}_1  > V_{tol},  \dot{d}_2  > V_{tol}$	0	$S_4 \rightarrow S_4$

Table 1: Table corresponding to the transition diagram in Fig. 4. The different types of transitions are I - Impact, C - Chatter, R - Release, L - Limit, T - Two-point impact, TR - Two-point impact with Release and TC - Two-point impact with Chatter.

380 A summary of all states and transitions are given in Table 1 and brief descriptions of the 16 transitions (I -  
381 XVI) in Fig. 4 are given here:

382 **Transition I.** Impact of end point  $P_1$  with  $|\dot{d}_1| > V_{tol}$ . The system will remain in free flight State 1.

383 **Transition II.** Impact of end point  $P_2$  with  $|\dot{d}_2| > V_{tol}$ . The system will remain in free flight State 1.

384 **Transition III.** If at impact  $|\dot{d}_1| < V_{tol}$ . The system will transition to stick State 2.

- 385 **Transition IV.** If at impact  $|\dot{d}_2| < V_{tol}$ . The system will transition to stick State 3.
- 386 **Transition V.** If at any moment during the constrained motion  $\ddot{d}_1 > 0$ , then the system will transition to free  
387 flight State 1.
- 388 **Transition VI.** If at any moment during the constrained motion  $\ddot{d}_2 > 0$  then the system will transition to free  
389 flight State 1.
- 390 **Transition VII.** In the limiting case where the impact angle  $\theta$  approaches zero with each impact and eventually  
391 reaches a predefined threshold in which the angle can be assumed to be zero. The system transitions to the  
392 symmetric State 4.
- 393 **Transition VIII.** If at impact  $\ddot{d}_1 > 0$  and  $\ddot{d}_2 < 0$ , then the system will transition to stick State 3.
- 394 **Transition IX.** If at impact  $\ddot{d}_2 > 0$  and  $\ddot{d}_1 < 0$ , then the system will transition to stick State 2.
- 395 **Transition X.** If at impact  $|\dot{d}_2| > V_{tol}$ , then the system transitions to the symmetric State 4.
- 396 **Transition XI.** If at impact  $|\dot{d}_1| > V_{tol}$ , then the system transitions to the symmetric State 4.
- 397 **Transition XII.** If at impact  $|\dot{d}_2| < V_{tol}$ , then the system will transition to the symmetric stick State 5.
- 398 **Transition XIII.** If at impact  $|\dot{d}_1| < V_{tol}$ , then the system will transition to the symmetric stick State 5.
- 399 **Transition XIV.** The system will remain in State 5 unless the frequency of oscillation exceeds a critical value  $\omega^*$   
400 given by  $\omega^* = \sqrt{\frac{g}{A \sin(\omega\tau)}}$ . When this value is exceeded the system will release from stick and transition to  
401 the symmetric State 4. For a given  $\omega$  value,  $\omega^*$  will vary sinusoidally depending on the phase of oscillation  
402  $\tau$ . When the floor acceleration is maximal,  $\omega^*$  will be minimized, and when the floor acceleration is minimal,  
403  $\omega^*$  will be maximized.
- 404 **Transition XV.** If  $\ddot{d}_{1,2} < 0$  or  $|\dot{d}_{1,2}| < V_{tol}$ , then the system will transition to the symmetric stick State 5.
- 405 **Transition XVI.** If at impact  $\ddot{d}_{1,2} > 0$ ,  $\dot{d}_1 > V_{tol}$  and  $\dot{d}_2 > V_{tol}$  the system will remain in State 4.

### 406 4.3. Results

407 Here we will focus on the numerical analysis of some aspects of the long-term dynamics of the impacting rod  
408 introduced in Section 4.1. The purpose of this is twofold. First, we want to show the robustness of the numerical  
409 techniques presented in Sections 4.1 and 4.2, and second, we want to display some of the behaviour that one can  
410 expect from a rattling object where energy that is dissipated both through the impact and friction. In this context  
411 we will focus both on steady-state dynamics and transients.

412 As discussed in Section 4.1 and shown in Fig. 3 the system can essentially be in five different states between  
413 events (impacts or transitions). On top of this numerical experiments have shown that the more energy that is  
414 removed from the system at impact through friction the faster the system tends from asymmetric to symmetric  
415 motion (see Fig. 5). In terms of the model example presented in this work, asymmetric chaos refers to chaotic  
416 motion when in State 1, and symmetric chaos refers to chaos when in State 4. This indicates that if the energy  
417 that is added into the system is acting in the normal direction relative to the impact then the friction, which only  
418 acts in the tangential direction, will reduce the rotational energy over time and only symmetric motion will remain.  
419 To highlight this the example in Fig. 5(a) shows a time history of the angle  $\theta$  when the system goes through a  
420 transition from asymmetric to symmetric motion. Recall that  $\theta = 0$  or  $\theta = \pi$  means that the rod is aligned parallel  
421 to the surface. In Fig. 5(b) we see a close up of how the actual transition in this case happens over a very short  
422 time interval. In principal it is an accumulation of alternative impacts between the two ends, i.e. very similar to  
423 what we see in complete chatter, but here we do not necessarily have stick. In Fig. 5(c) we see a similar example,  
424 where the time history of the position of each of the two end points are shown to highlight how the transition  
425 between transient asymmetric chaos and transient symmetric chaos can occur. We note that up to approximately  
426  $t = 302$  there are two separate trajectories, one for each end point, but suddenly the two trajectories converge and  
427 the two end points move in synchrony and the rotation of the rod ends. The figure also indicates that the system  
428 stays chaotic but where all the rotational energy has dissipated due to friction. This will not always be the case  
429 however, as seen in Figs. 6 (a) and (b). After  $t = 790$  the system still remains in asymmetric chaos. A comparison  
430 of Fig. 6 (b) with Fig. 5(c) shows the difference between asymmetric and symmetric chaos. In Fig. 6 (b) the system

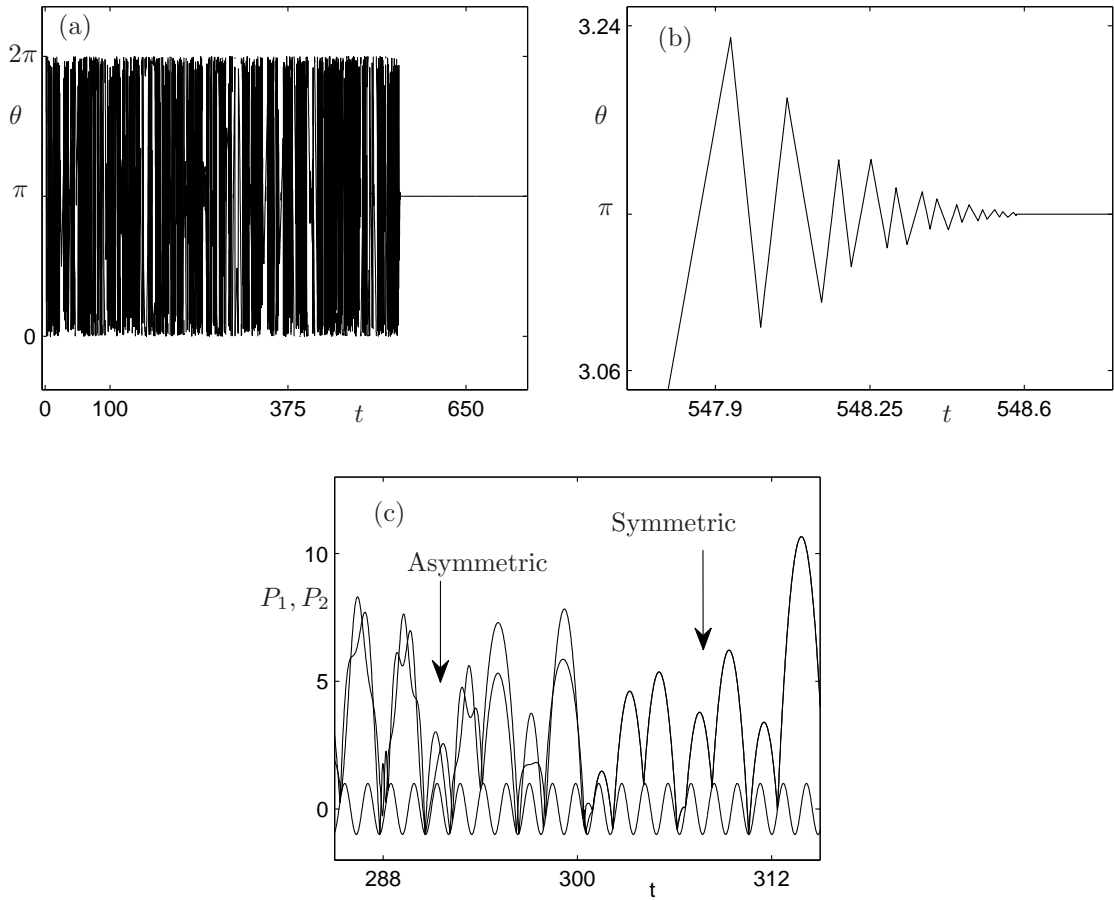


Figure 5: Time histories showing (a) the rod angle  $\theta \bmod 2\pi$ , (b) a close-up of (a) showing the transition from asymmetric to symmetric motion, and (c) the surface  $S(t)$  and the end points  $P_1(t)$  and  $P_2(t)$  for the rod before and after the transition from asymmetric to symmetric motion occurs. Here  $\omega = 4.4050$ ,  $e_* = 0.8$ ,  $A = 1$  and  $\mu = 0.05$ .

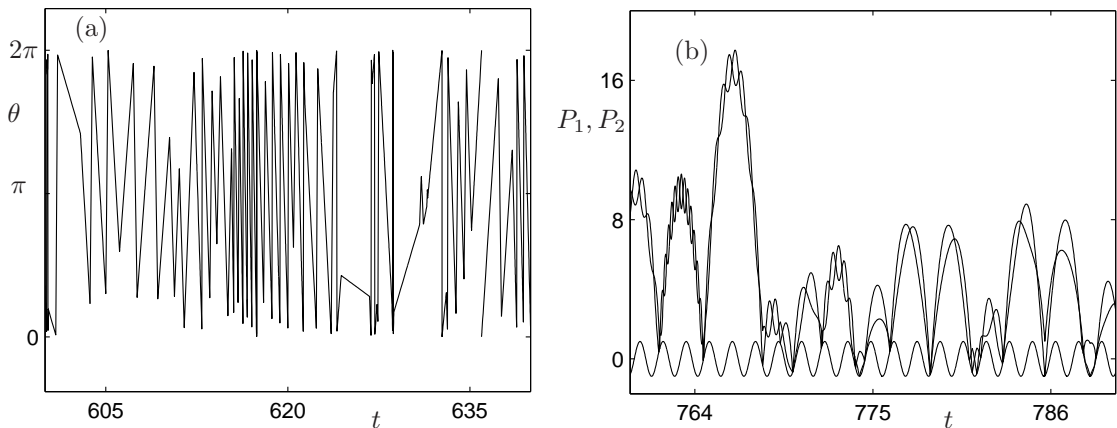


Figure 6: Time histories showing (a) the rod angle  $\theta \bmod 2\pi$  and (b) the contact points  $P_1(t)$  and  $P_2(t)$  for  $\omega = 4.40572$ ,  $e_* = 0.9$ ,  $A = 1$  and  $\mu = 0.5$ .

431 has still not reached symmetric chaos (transitioned to state 4) and it is possible that it never will. In Fig. 5(c) the  
 432 system has reached symmetric chaos (transitioned to state 4).

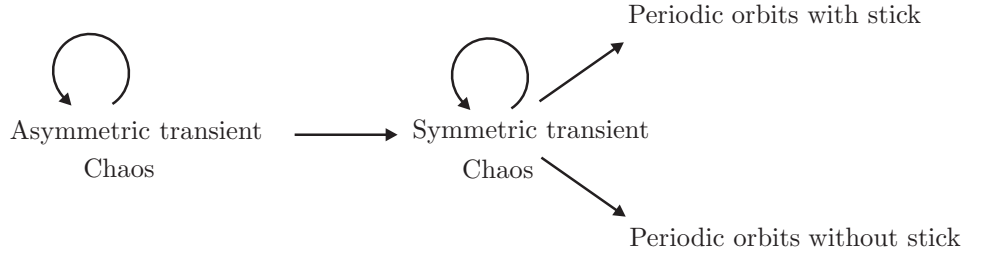


Figure 7: A schematic detailing the possible transitions from transient asymmetric chaos to transient symmetric chaos and periodic orbits that can occur in the system.

433 In Fig. 7 a schematic transition diagram for transient motions found in the rod system is shown. Note that this  
 434 schematic is based on observations from numerical experiments of the rod system and not on analytically derived  
 435 conditions. In many cases, for general initial conditions, the rod system undergoes motion akin to asymmetric  
 436 chaos until the rotational energy has dissipated and the symmetric (transient) chaos takes over. Depending on the  
 437 frequency of the external forcing the symmetric chaos may persist or the motion turn periodic. Again, depending  
 438 on the frequency and the value of the restitution coefficient the periodic orbits may have periods of stick. The  
 439 effect of this is that, at least for low frequencies  $\omega$ , all long term motions that we have come across, are symmetric  
 440 and thus brute-force bifurcation diagrams only show stable solutions, where the dynamics is symmetric. It is worth  
 441 noting that in the limit, where the impact times between the end points as well as the tangential impact velocities  
 442 go to zero, Map I (see Section 2.2) is successively applied and once the transition to symmetric motion has occurred  
 443 Map I reduces to the standard Newtonian restitution law, which is in-line with what is discussed in [28]. For the  
 444 rod system in question this means that the long term behavior can simply be approximated by a one-dimensional  
 445 system of a mass impacting an oscillating surface. While the general one-dimensional system has been analysed  
 446 before, see particularly Holmes [20], we will present some specific results for the system analysed here in order to  
 447 give us an idea on what we can predict regarding the long-term behaviour for specific parameter values.

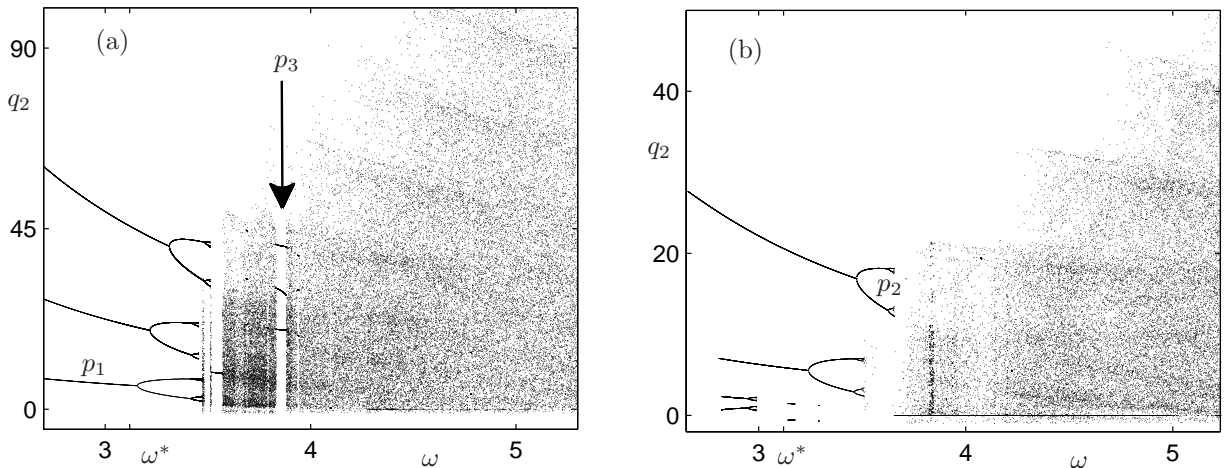


Figure 8: Bifurcation diagrams showing how the steady-state of the position of the centre of mass  $q_2$  varies as the frequency  $\omega$  is varied. In (a)  $e_* = 0.9$ ,  $A = 1$  and  $\mu = 0.05$  and in (b)  $e_* = 0.8$ ,  $A = 1$  and  $\mu = 0.05$ . The period-1 orbit is labeled in (a) and the period-2 and period-3 orbits are labeled in (b).

448 To describe how possible transitions between different types of long-term motion in the symmetric (one-  
 449 dimensional) rod system occur we show in Fig. 8 (a) and (b) two brute-force bifurcation diagrams,  $\omega$  vs.  $q_2$ ,  
 450 for two different values of the restitution coefficient,  $e_* = 0.9$  and  $e_* = 0.8$ , respectively. Fig. 8(a) shows three coex-  
 451 isting period-1 solutions that undergo period-doubling sequences, at three different values of  $\omega$ , until the branches  
 452 disappear in grazing bifurcations at  $\omega \approx 3.5$ . The figures also shows that regions of chaos start at  $\omega \approx 3.5$ , with two  
 453 periodic windows (a period-1 and a period-3 orbit, see Fig. 9(a)) also existing within the chaos. The bifurcation

454 diagram in Fig. 8(b), where the restitution coefficient is lower, we see that the onset of chaos occurs at  $\omega \approx 3.8$   
455 and thus the periodic orbits are sustained longer when more energy is taken out of the systems at impact. To show  
456 what some of the symmetric period-1 solutions look like in Fig. 9(a) a time series of the end points of the period-1  
457 orbit highlighted as  $p_1$  in Fig. 8(a) ( $p_1$ ) is shown. In Fig. 9(b) a time series of the end points of the period-2  
458 orbit highlighted as  $p_2$  in Fig. 8(b) is shown. Similarly in Fig. 9(c) a time series of the end points of the period-3  
459 orbit highlighted as  $p_3$  in Fig. 8(a) is shown. This shows that freely rattling objects subject to periodic forcing  
460 have co-existing recurrent motions, periodic and/or chaotic, as has been shown before [20]. The three co-existing  
461 period-1 orbits in Fig. 8(a) are reached from different initial conditions, i.e. the rod system is initially impacting  
462 the surface at different phases of the surface oscillation. The time history illustrated in Fig. 9 (c) corresponds to  
463 initial conditions taken from the the period-1 orbit in Fig. 8.

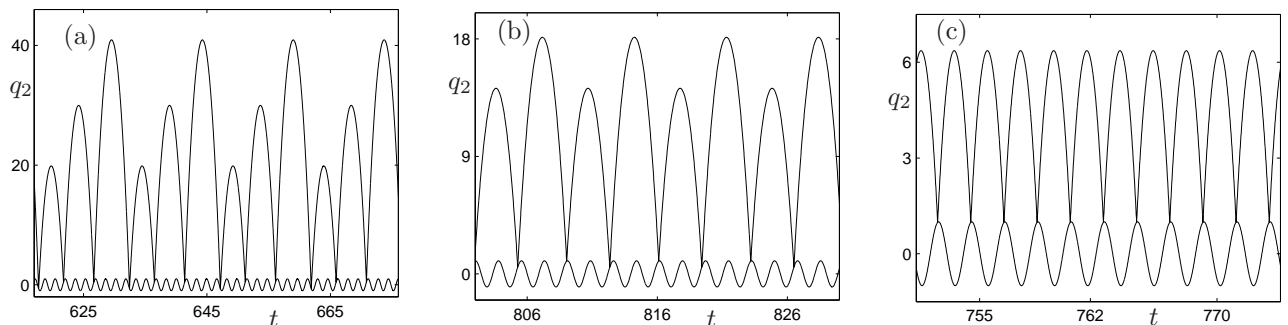


Figure 9: Time histories for  $q_2$  showing (a) a period-3 solution (see label  $p_3$  in Fig. 8(a)), (b) a period-2 solution (see label  $p_2$  in Fig. 8(b)) and (c) a period-1 solution (see label  $p_1$  in Fig. 8(a)). In (a) and (c)  $\omega = 3.0$ ,  $e_* = 0.9$ ,  $A = 1$  and  $\mu = 0.05$  and in (b)  $\omega = 3.55085$ ,  $e_* = 0.8$ ,  $A = 1$  and  $\mu = 0.05$ .

464 A useful technique for understanding the long-term behaviour in this system is to examine how the period-1  
465 solutions behave under parameter variations. In Fig. 10(a) we plot bifurcation diagrams using continuation methods  
466 for five different  $e_*$  values under  $\omega$  variation. The figure shows that period-1 orbits are born at a smaller frequency  
467  $\omega$  the bigger the  $e_*$  value is. It seems obvious that if less energy is taken out at impact then less energy is needed  
468 from the oscillating surface to sustain a similar periodic orbit. In the inset I we highlight how the branches of  
469 periodic orbits retract as  $e_*$  is increased. In Fig. 10(b) we show a magnification of the region II in Fig. 10(a)  
470 to highlight that the stable branches born at saddle-node bifurcations (SN) undergo period-doubling bifurcations  
471 (PD) for increasing  $\omega$ , which we also see in Fig. 8(a). Figure 10(b) also shows how the unstable periodic orbits  
472 born at SN bifurcations disappear at grazing bifurcations (G). As mention above, these results are qualitatively in  
473 agreement with what is presented in [20]. The conclusion of this is that if the set of parameters are such that they  
474 lie to the left of the corresponding saddle-node bifurcation SN in Fig. 10(b) the long-term motion is stick and if  
475 they lie to the right of the period-doubling bifurcation PD the long-term motion is symmetric period- $n$  ( $n > 1$ ) or  
476 symmetric chaos. If the set of parameters are such the system is in-between SN and PD we can expect symmetric  
477 period-1 orbits in the long term.

## 478 5. Discussion

479 In this paper we introduced a framework for the numerical simulation of rigid-body systems with impacts and  
480 friction, specifically using the impact maps first derived in [28]. We present the framework for a general one-point  
481 rigid-body collision and show how the impact maps derived in [28] can be extended to allow for an impact between  
482 two unconstrained rigid bodies. Further we implemented the impact maps in a hybrid simulation environment in  
483 MATLAB, allowing for simulation of long-term dynamics of a planar rod where the two end points can impact an  
484 oscillating surface. For this purpose we introduced a framework that includes an ODE solver, system states and  
485 a transition diagram. This allowed us to reliably simulate the system in free flight, through impacts, in sticking  
486 and through complete chatter. For instance, the approach involved switching vector fields when the system is  
487 transitioning between stick and free flight motion, where the vector field for stick was found by calculating the  
488 normal force required to constrain the contact point to the surface.

489 In Table 1 together with Fig. 4 we presented a summary of what is needed to detect an event and what state  
490 transition the system will encounter. One of the shortcomings of our approach, and an area of future research, is

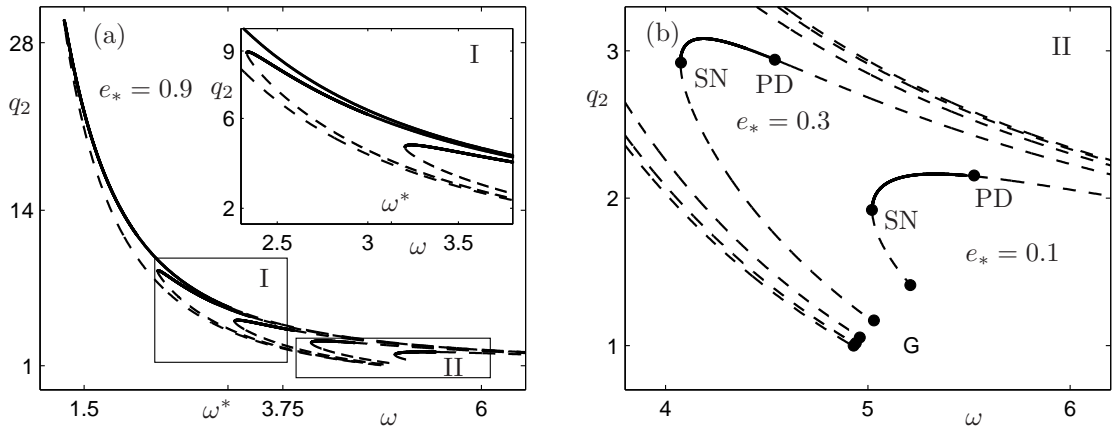


Figure 10: Bifurcation diagrams showing how the period-1 solution labeled  $p_1$  in Fig. 8(a) varies with  $\omega$  when  $e_* = 0.9, 0.7, 0.5, 0.3$  and  $0.1$ . Solid line represents the stable limit cycles and the dashed lines represent unstable limit cycles. In (a) all the branches are shown along with a magnification in panel I to further detail the structure. In (b) a magnification of panel II in (a) is shown. It highlights where the SN, PD and G bifurcations occur.

491 that we end a complete chattering sequence when the contact point velocity reaches an a priori defined velocity  
492 threshold  $V_{tol}$ , albeit small. This is in contrast to the method that was derived in [31] for impacts without friction,  
493 where at the end of a complete chatter sequence a jump in space and time is done to minimize local numerical  
494 errors. An improvement here would be to extrapolate through chatter sequences, using a similar approach as in  
495 [31], until the relative velocity is zero. Another related issue that is not fully resolved in this paper is in the limiting  
496 case whereby two impact events accumulate, and in our case where the rod angle  $\theta$  approaches zero. In this case  
497 we, again, define a tolerance  $\theta_{crit}$  a priori for when the transition from asymmetric to symmetric motion should  
498 occur. This was necessary to ensure robustness in the numerical scheme.

499 As mentioned above, we implemented this framework for the model example of a slender rod impacting a  
500 periodically forced surface. This example highlighted some of the phenomena present in impacting systems with  
501 friction, and in particular symmetric systems. The model example can, in some sense, be likened to the problem  
502 of machine rattle, whereby a machine element becomes detached and is free to undergo unconstrained mechanical  
503 vibration. For the rod system we examined the dynamics under variation of the frequency of surface oscillation  
504  $\omega$ . We showed that for high values of the restitution coefficient and low frequencies multiple periodic solutions  
505 coexist, however they do not survive an increase in  $\omega$ , but instead chaotic regimes take over. Another aspect that  
506 was highlighted for low frequencies  $\omega$  is how friction removes rotational energy so that mainly symmetric motions  
507 (impacts of both end points of the rod at the same time) persists. One of the main limitations of the symmetric  
508 rod system is that once it is in symmetric motion it can not get back to asymmetric motion. If an external torque  
509 was included or if the bar was not completely uniform then such a transition could occur and most likely make the  
510 system even more unpredictable. Although both generalisations would be possible to implement, they have not  
511 been considered for this work since the main goal was to introduce a framework for simulating long-term dynamics  
512 for a rigid-body system with impacts and friction and to highlight some interesting features that can be observed  
513 through long-term simulations.

514 The model example we chose to illustrate our techniques, albeit a simple geometry, was entirely unconstrained.  
515 Incorporating a more complex geometry, with more contact points, but with one or more constraints, would lead to  
516 a less complicated transition diagram than the one presented in Fig. 4. The advantage of the techniques presented  
517 in this paper is that they can be easily extended to and implemented for other mechanical systems, with relatively  
518 few contact points, where impacts and stick motions can occur. The implementation of our method would become  
519 increasingly difficult for an unconstrained system with more than two contact points, and it then may be necessary  
520 to consider a time-stepping scheme. However, it would then not be possible to perform the careful stability analysis  
521 techniques illustrated in this article. Further, the numerical scheme does not need to handle large number of events  
522 at one time and it is possible to deal with complete chatter sequences. The algorithm described here can also be  
523 exported directly to methods that locate periodic orbits and determine their stability using a shooting method,  
524 which is the only useful method to date that can be used for periodic orbits with incomplete or complete chatter.

525 This article has opened up new research questions regarding numerical methods, as mentioned above, but also

526 the exact role friction has in dissipating rotational energy in general rattling objects. It may be possible to find  
527 a relationship between the energy removed due to friction and the energy introduced into the system through the  
528 periodic forcing. Such analysis may be a useful predictive tool for engineers working with unconstrained impacting  
529 systems with friction.

## 530 Acknowledgments

531 SB wishes to acknowledge the economic support from the National University of Ireland, Galway (NUI Galway)  
532 through a PhD scholarship in applied mathematics.

- 533 [1] Acary, V., Brogliato, B., 2007. Numerical methods for nonsmooth dynamical systems: Applications in Me-  
534 chanics and Electronics. Vol. 35. Springer-Verlag.
- 535 [2] Adolfsson, J., Dankowicz, H., Nordmark, A., 2001. 3D passive walkers: Finding periodic gaits in the presence  
536 of discontinuities. *Nonlinear Dynamics* 24, 205–229.
- 537 [3] Alzate, R., di Bernardo, M., Montanaro, U., Santini, S., 2007. Experimental and numerical verification of  
538 bifurcations in cam-follower systems. *Journal of Nonlinear Dynamics* 50, 409–429.
- 539 [4] Alzate, R., Piiroinen, P. T., di Bernardo, M., 2012. From complete to incomplete chattering: a novel route to  
540 chaos in impacting cam-follower systems. *International Journal of Bifurcation and Chaos* 22 (5), 409–429.
- 541 [5] Barthel, E., 2008. Adhesive elastic contacts: JKR and more. *Journal of Physics D: Applied Physics* 41, 1–20.
- 542 [6] Brach, R. M., 1993. Classical planar impact theory and the tip impact of a slender rod. *International Journal of*  
543 *Impact Engineering* 13 (1), 21–33.
- 544 [7] Brach, R. M., 2007. *Mechanical Impact Dynamics, Rigid Body Collisions*. John Wiley & Sons, New York.
- 545 [8] Brogliato, B., 2007. *Nonsmooth Mechanics*. Springer-Verlag.
- 546 [9] Budd, C. J., Dux, F., 1994. Chattering and related behaviour in impact oscillators. *Philosophical Transactions*  
547 *of the Royal Society of London A* 347, 365–389.
- 548 [10] Budd, C. J., Piiroinen, P. T., 2006. Corner bifurcations in non-smoothly forced impact oscillators. *Physica D*  
549 220, 127–145.
- 550 [11] Burns, S. J., Piiroinen, P. T., 2014. The complexity of a basic impact mapping for rigid bodies with impact  
551 and friction. *Journal of Regular and Chaotic dynamics* 19 (1), 20–36.
- 552 [12] Chillingworth, D., 2002. Discontinuity geometry for an impact oscillator. *Dynamical Systems* 17, 380–420.
- 553 [13] Dankowicz, H., Piiroinen, P. T., 2002. Exploiting discontinuities for stabilization of recurrent motions. *Dy-*  
554 *namical Systems* 17, 317–342.
- 555 [14] di Bernardo, M., Budd, C. J., Champneys, A. R., Kowalczyk, P., 2007. *Bifurcation and Chaos in Piecewise*  
556 *Smooth Dynamical Systems- Theory and Applications*. Springer-Verlag.
- 557 [15] di Bernardo, M., Budd, C. J., Champneys, A. R., Kowalczyk, P., 2008. *Piecewise Smooth Dynamical Systems*  
558 *– Theory and Applications*. Springer-Verlag, London UK.
- 559 [16] Fredriksson, M., Nordmark, A., 2005. Oblique frictional impact of a bar: Analysis and comparison of different  
560 impact laws. *Nonlinear Dynamics* 41, 361–383.
- 561 [17] Génot, F., Brogliato, B., 1999. New results on painlevé paradoxes. *European Journal of Mechanics A/Solids*  
562 18, 653–677.
- 563 [18] Ghajari, M., Galvanetto, U., Iannucci, L., Willinger, R., 2011. Influence of the body on the response of the  
564 helmeted head during impact. *International Journal of Crashworthiness* 16 (3), 285–295.
- 565 [19] Goldsmith, W., 2001. *Impact: The theory and physical behaviour of colliding solids*. Dover Publications.
- 566 [20] Holmes, P. J., 1982. The dynamics of repeated impacts with a sinusoidally vibrating table. *Journal of Sound*  
567 *and Vibration* 84 (2), 173–189.

- 568 [21] Ivanov, A. P., 1992. Energetics of a collision with friction. *Journal of Applied Mathematics and Mechanics* 56,  
569 527–534.
- 570 [22] Keogh, P. S., Cole, M. O. T., 2003. Rotor vibration with auxiliary bearing contact in magnetic bearing systems  
571 part 1: synchronous dynamics. *Journal of Mechanical Engineering Science* 217 (4), 377–392.
- 572 [23] Leine, R. I., Brogliato, B., Nijmeijer, H., 2002. Periodic motion and bifurcations induced by the painlevé  
573 paradox. *European Journal of Mechanics A/Solids* 21, 869–896.
- 574 [24] Leine, R. I., Nijmeijer, H., 2004. Dynamics and bifurcations of non-smooth mechanical systems. *Lecture Notes  
575 in Applied And Computational Mechanics* 18.
- 576 [25] Leine, R. I., Van Campen, D. H., Glocker, C. H., 2003. Nonlinear dynamics and modelling of various wooden  
577 toys with impact and friction. *Journal of Vibration and Control* 9 (1-2).
- 578 [26] Mason, J., Homer, M., Wilson, R. E., 2007. Mathematical models of gear rattle in roots blower vacuum pumps.  
579 *Journal of Sound and Vibration* 308, 431–440.
- 580 [27] Nordmark, A., 2001. Existence of periodic orbits in grazing bifurcations of impacting mechanical oscillators.  
581 *Nonlinearity* 14, 1517–1542.
- 582 [28] Nordmark, A., Dankowicz, H., Champneys, A., 2009. Discontinuity-induced bifurcation in systems with im-  
583 pacts and friction: Discontinuities in the impact law. *International Journal of Non-Linear Mechanics* 44,  
584 1011–1023.
- 585 [29] Nordmark, A., Dankowicz, H., Champneys, A., 2011. Friction-induced reverse chatter in rigid-body mecha-  
586 nisms with impacts. *IMA Journal of Applied Mathematics* 76, 85–119.
- 587 [30] Nordmark, A. B., 1991. Non-periodic motion caused by grazing incidence in impact oscillators. *Journal of  
588 Sound and Vibration* 2, 279–297.
- 589 [31] Nordmark, A. B., Piiroinen, P. T., 2009. Simulation and stability analysis of impacting systems with complete  
590 chattering. *Nonlinear Dynamics* 58, 85–106.
- 591 [32] Osorio, G., D. B. M., Santini, S., 2005. Chattering and complex behaviour of a cam-follower system.
- 592 [33] Pfeiffer, F., Glocker, C., 2004. *Multibody Dynamics with Unilateral Contacts*. WILEY-VCH.
- 593 [34] Piiroinen, P. T., Dankowicz, H. J., 2005. Low-cost control of repetitive gait in passive bipedal walkers. *Inter-  
594 national Journal of Bifurcation and Chaos* 15 (6), 1959–1973.
- 595 [35] Piiroinen, P. T., Dankowicz, H. J., Nordmark, A. B., 2003. Breaking symmetries and constraints: Transitions  
596 from 2D to 3D in passive walkers. *Multibody System Dynamics* 10, 147–176.
- 597 [36] Piiroinen, P. T., Kuznetsov, Y. A., 2008. An event-driven method to simulate filippov systems with accurate  
598 computing of sliding motions. *ACM Transactions on Mathematical Software* 34 (3).
- 599 [37] Stronge, W. J., 1990. Rigid body collisions with friction. *Mathematical and Physical Sciences* 431 (1881),  
600 169–181.
- 601 [38] Stronge, W. J., 2000. *Impact Mechanics*. Cambridge University Press.
- 602 [39] Wang, Y., Mason, M. T., 1992. Two-dimensional rigid-body collisions with friction. *Journal of Applied Me-  
603 chanics* 59, 635–642.
- 604 [40] Zhao, Z., Liu, C., Brogliato, B., 2009. Planar dynamics of a rigid body system with frictional impacts. II.  
605 qualitative analysis and numerical simulations. *Proceedings of the Royal Society A* 465, 2267–2292.